

Magnetic properties of ultrafine-grained cobalt samples obtained from consolidated nanopowders

F. Fellah¹, S. M. Chérif^{*1}, K. Bouziane², F. Schoenstein¹, N. Jouini¹, and G. Dirras¹

¹LSPM (CNRS-UPR 3407), Université Paris 13, 99 av. J.B. Clément, 93430 Villetaneuse, France

²Department of Physics, College of Science, Sultan Qaboos University, P.O. Box 36, Al-Khodh 123, Sultanate of Oman

Received 16 August 2010, revised 5 March 2011, accepted 11 March 2011

Published online 1 April 2011

Keywords cobalt, inelastic light scattering, magnetic properties, nanopowders

* Corresponding author: e-mail cherif@univ-paris13.fr, Phone: +33 1 49 40 34 73, Fax: +33 1 49 40 39 38

Co powders having nominal average particle size of 50 and 240 nm were synthesized using a polyol method and then consolidated by hot isostatic pressing (HIP) or the emerging spark plasma sintering (SPS) compaction processes. Bulk polycrystalline aggregates were obtained, having average grain sizes of about 200 and 300 nm, respectively. It is found that both nanoparticles and consolidated samples exhibit a soft ferromagnetic behavior. The magnetization reversal likely occurs by

nucleation/propagation process. However, a curling process can be involved in the magnetization reversal for the smaller particles. The dynamic measurements provide for the consolidated samples magnetic parameters corresponding to bulk cobalt with vanishing anisotropy. The contribution of the intergranular region is found to be negligible. We can infer that the used consolidation routes insure a good magnetic interfacial contact between the particles.

© 2011 WILEY-VCH Verlag GmbH & Co. KGaA, Weinheim

1 Introduction With the reduction of the grain size, materials properties are enhanced in many fields of physics. It is now established that the morphology, size of the crystallites and the intercrystallite interactions greatly influence various properties in nanostructured material [1, 2]. Two strategies to elaborate nanostructured materials are usually used and are referred to as “top down” and “bottom up.” The first one consists on reducing grains size by introducing deformation in a bulk with techniques of so-called severe plastic deformation (SPD) [3, 4]. The second one consists of elaborating a dense material by aggregation of atoms such as electrodeposition [5] or by compacting nanoparticles using powder metallurgy (PM) techniques.

The magnetic response of a material is highly influenced by its microstructure in addition to its shape and size. These factors depend on the processing route [6]. The elaboration of bulk nanostructured metal via a bottom-up strategy combining sol-gel method and consolidation by hot isostatic pressing (HIP) [7] or the emerging spark plasma sintering (SPS) [8] has proved recently to be a promising approach in order to obtain ultrafine-grained materials showing specific interesting properties. Some interesting papers report studies of magnetic properties of powdered and consolidated soft

amorphous materials [9, 10] mainly dealing with the static behavior of magnetization. The study of the microstructure–property relationship in soft magnetic nanocrystalline Fe-based materials pointed out the key role of the magnetocrystalline and exchange interaction [11]; the resulting magnetic behavior is well described with the random anisotropy model (RAM) [12] initially proposed by Alben et al. [13]. The basic mechanism for the soft magnetic behavior is that the local magnetocrystalline anisotropies are randomly averaged out for grain sizes smaller than the ferromagnetic exchange length, with the consequence that the coercive field H_c decreases with decreasing the grain size D . For amorphous materials or for nanocrystalline materials (up to $D = 100$ nm), a D^6 dependence of H_c is observed [11]. The nanocrystalline materials fill in the gap between amorphous and conventional polycrystalline materials that exhibit large grain size, for which H_c follows a $1/D$ dependence [11]. The RAM has also been successfully applied to nanostructured transition metals [14, 15] and coarse-grained polycrystalline alloys [16]. The $1/D$ behavior of the coercive field is usually explained by domain-wall pinning at grain boundaries. For large grain size and for bulk magnetic materials, a magnetization reversal taking place

through a process of nucleation of small reversed domains (usually on inhomogeneities or defects) and a subsequent propagation of magnetic domain walls is rather reported [17]. The magnetic properties may also be affected by local structural features in the grain boundaries [18, 19]. On the other hand, the exchange coupling between the grains also depends on the magnetic nature of the intergranular region, as observed in multiphase systems [11].

In this work, we mainly report on the study of both the static and dynamic magnetic properties of synthesized Co nanoparticles and the corresponding ultrafine-grained aggregates, with sizes lying in an intermediate range between nanocrystalline and microcrystalline materials, namely between 200 and 300 nm, obtained by the nonconventional consolidation SPS and HIP techniques. The first objective is to verify the variation of magnetic properties, if any, upon consolidation of Co nanoparticles and to point out the role of the intergranular region. The elaboration processes, the structural and morphological properties are briefly presented and commented on. Details are presented elsewhere [20, 21]. The hysteresis loops for the Co nanoparticles were obtained using a magnetic balance of the Faraday type. Vibrating sample magnetometry (VSM) and Brillouin light scattering (BLS) spectroscopy techniques have been used in order to investigate, respectively, the static and dynamic magnetic behavior of the Co consolidated materials.

2 Samples and experimental tools Co nanoparticles have been synthesized by the polyol method using nucleant agent [22]. Depending on the nature and the concentration of the nucleant agent, two cobalt particle average sizes were obtained: 50 and 240 nm. The experimental procedure is as follows: first, ionic salts, cobalt (II) acetate tetrahydrate (0.02 and 0.08 mol/L, respectively), sodium hydroxide (0.05 and 0.2 mol/L, respectively) and K_2PtCl_4 (0.08 mmol/L), and $AgNO_3$ (0.04 mmol L^{-1}) were dissolved in 1,2-propanediol. Then the solution was heated up at boiling point (186°C) for 6 h under mechanical stirring and distillation. After cooling to room temperature, Co nanoparticles were separated from the supernatant by centrifugation and washed with ethanol and acetone. Finally, dense nanostructured materials were obtained using SPS (model 515S of Syntex society) and HIP techniques. The SPS sintering was carried out under a pressure of about 50 MPa and at a temperature of 500°C for 150 s at the sintering temperature. HIP sintering was processed at a

temperature of 500°C and a pressure of 200 MPa for 2 h. The studied samples are finally prepared in the form of thin plates.

The crystalline phase assemblies present in the powdered and in the compacted materials were determined by X-ray powder diffraction [X-ray diffraction (XRD)] using $CoK_{\alpha 1}$ radiation whose wavelength is 1.78896 \AA . Microstructural investigations of the as-prepared powders and of as-consolidated specimens were conducted on a JEOL 2011-EFTEM transmission electron microscope, operated at 200 kV. The grain sizes of these materials were determined from TEM micrographs by measuring and averaging the diameters of more than 150 grains. The magnetization of the consolidated samples was measured with a DMS 1660 VSM in a magnetic field up to 13.5 kOe applied in-plane (longitudinal configuration) and out-of-plane (polar configuration). The VSM was calibrated using pure nickel ($M_s = 54.9 \text{ emu/g}$). The dynamic properties of the consolidated films were studied by means of the BLS technique that constitutes a powerful tool to investigate the magnetic properties of magnetic films [23, 24]. In a BLS experiment, a beam of Ar^+ laser light operated on a single mode of the 514.5 nm line, is used as a probe to reveal spin waves that are naturally present in the medium under investigation in the 3–300 GHz spectral frequency range. A 300-mW p-polarized light was focused on the surface of the sample and the scattered light was analyzed by means of a Sandercock-type 3 + 3 pass tandem Fabry–Pérot interferometer. In the present work, we used the backscattering geometry so that the value of the wave vector of the spin waves probed is fixed experimentally to the value $k = (4\pi/\lambda)\sin\theta$, where λ denotes the wavelength in air of the laser light and θ the angle of incidence. Moreover, the excited spin waves are studied versus the amplitude of the in-plane applied magnetic field up to 5 kOe.

3 Results and discussion

3.1 Structure and morphology For simplicity, the consolidated samples were labeled according to the initial size of particles and the compression method used, namely SPS50, SPS240, and HIP240 (see Table 1).

Figure 1 shows typical XRD patterns corresponding to the 50-nm powder (a) and SPS50 consolidated sample (b). The quantitative analysis of the crystalline phases showed that the 50-nm powder XRD pattern exhibits mainly ($\approx 100\%$) a face-centered cubic (fcc) structure while a

Table 1 Grain size: D , saturation magnetization M_s , remanent magnetization M_r , squareness S , and coercive field: H_c , measured on nanoparticles and ultrafine grains consolidated samples.

samples	D (nm)	M_s (emu/g)	M_r (emu/g)	$S = M_r/M_s$	H_c (Oe)
50-nm particles		145	8	0.055	100
240-nm particles		165	4	0.024	50
SPS50	235	165	5	0.03	40
SPS240	280	165	21	0.13	70
HIP240	310	165	25	0.15	100

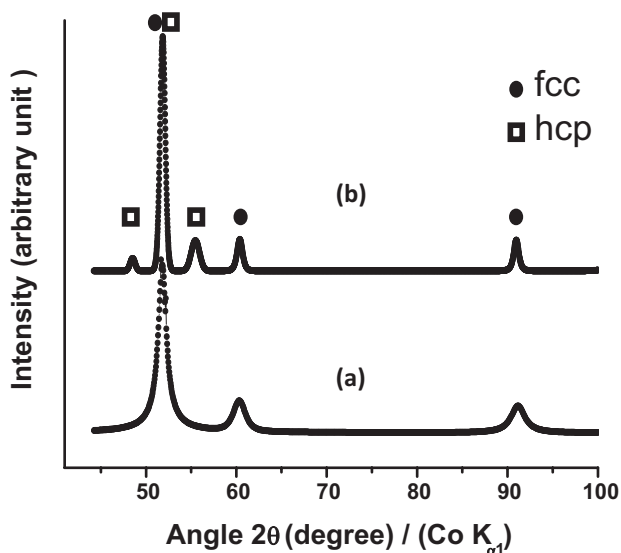


Figure 1 XRD spectra of 50 nm Co powders (a) and SPS50 consolidated sample (b).

hexagonal close-packed (hcp) structured phase ($\approx 15\%$) is also observed for the 240-nm particles (not shown). After compaction we notice an increase of the hcp structured phase (until 35%) as observed on Fig. 1b. Figure 2 shows the TEM microstructures of the 50-nm powder (a) and the corresponding size distribution of the particles (b).

One can observe that the powder consists of spherical particles with a narrow size distribution. For the corresponding consolidated sample (Fig. 3a), the average grain size D is larger, namely $D = 235$ nm (Fig. 3b). For the investigated consolidated samples, D scales in the range of 200–300 nm: 235, 280 and 310 nm for the SPS50, SPS240, and HIP240, respectively (Table 1). It is noticed here that the grain growth strongly depends on both the initial particle size and the processing route. For the SPS processing the grain sizes in the bulk samples are about 340 and 16% for the 50 and 240-nm powders, respectively. For the HIP processing of the 240-nm powder the grain size is about 22%, *i.e.*, 4% higher than observed for the SPS counterpart. Nevertheless, in this case, the temperature, the pressure and time are important parameters. More generally, grain growth during sintering happens due to motion of atoms across a grain boundary. Convex surfaces have a higher chemical potential than concave surfaces, therefore grain boundaries will move toward their center of curvature. This is the situation of relatively smaller particles that are characterized by a higher radius of curvature and then a larger grains growth is expected. The relative densities measured by the Archimedes method are 91.4, 74.5, and 91.3% for the SPS50, SPS240, and HIP240 samples, respectively. Indeed, all compacted materials are still porous. This difficulty to obtain fully dense materials starting from nanopowder is frequently reported in literature [25]. As shown by the TEM micrographs the core of each individual grain exhibits a highly faulted nanoscaled lamellar microstructure (for

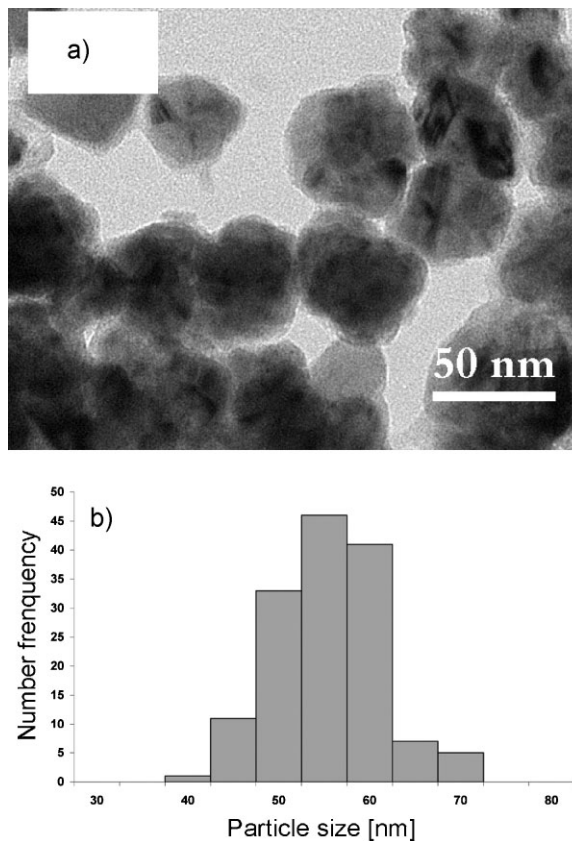


Figure 2 TEM photomicrographs of 50-nm Co powders (a) and corresponding size-distribution histogram (b).

instance, see Fig. 3a) composed of an intricate mixture of fcc, hcp structures, and nanotwins. More details can be found in Ref. [20]. It is possible that these thin microstructures, of less than 10 nm thickness, might induce a local preferential direction of the magnetocrystalline anisotropy axis within each grain, thus influencing magnetic properties.

3.2 Static magnetic measurements

3.2.1 Nanoparticles Figure 4 displays hysteresis loops, magnetization M versus applied field H , at RT for the 50- and 240-nm size Co particles. The related values of coercive field H_c and of squareness S , defined as the ratio of the remanent magnetization M_r to the saturation magnetization M_s , are reported in Table 1. The coarser particles exhibit a weaker H_c (≈ 50 Oe) than the smaller ones (≈ 100 Oe) and a higher M_s (165 vs. 145 emu/g) typical of bulk characteristics [26]. Surface oxidation or, as previously observed, residual solvent molecules adsorbed on the surface [27, 28] could explain the observed reduction of M_s for the small particles relative to the bulk value. Note that the in-plane H_c values are sensitively higher than those reported for thick cobalt films (few Oe) [29]. On the other hand, the enhancement of the coercivity for the smaller nanoparticles is in agreement with the results reported for Ni nanoparticles [30] and those of Leslie-Pelecky and Rieke [31] linking the maximum of H_c

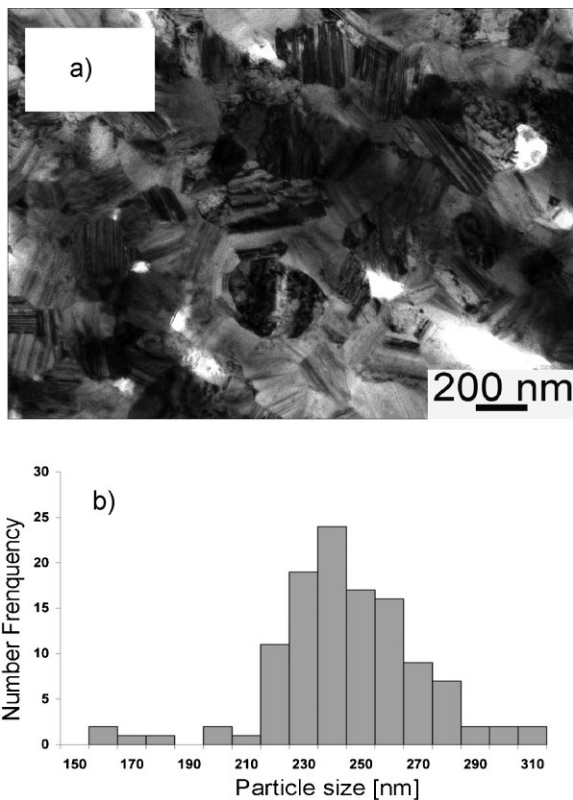


Figure 3 SPS50 consolidated sample (a) and corresponding size distribution histogram (b).

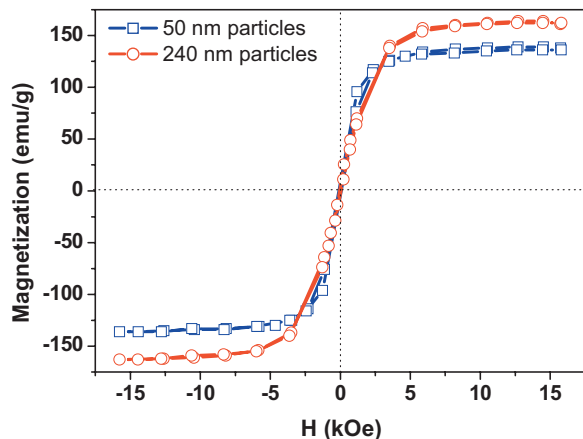


Figure 4 (online colour at: www.pss-a.com) Hysteresis loops of 240-nm (○) and 50-nm (□) cobalt nanopowders obtained at room temperature ($T = 300$ K).

value to the critical diameter d_c . It is worth noting that for both Co particles the magnetization saturation is achieved with a high applied field $H_s \approx 5$ kOe, which approximately corresponds to the demagnetizing field of a single supposed spherical particle: $4\pi M_s/3$, with $4\pi M_s = 17.6$ kOe (*i.e.*, 165 emu/g) the saturation magnetization of bulk cobalt. This emphasizes the role of the dipolar interactions between particles.

The mechanisms responsible for the magnetization reversal can correspond to coherent rotation, curling or domain-wall motion. In the case of a spherical nanoparticle of diameter D , Aharoni has shown that the process of magnetization reversal by coherent rotation is ensured for up to a diameter such that $D < d_c = 7.21\Lambda$, Λ being the exchange length given by $(A/2\pi M_s^2)^{1/2}$; with A the exchange stiffness constant [32]. Namely, using the cobalt material parameters determined from our BLS measurements as discussed in Section 3.3 ($A = 1.8 \times 10^{-6}$ erg/cm and $4\pi M_s = 17.6$ kOe, *i.e.*, 165 emu/g), one finds $\Lambda \approx 4$ nm, in good agreement with the literature [33]. We can conclude that the homogeneous rotation is then operative up to approximately a particle diameter of about 30 nm. Since the diameters of our particles are above the critical size d_c for coherent rotation, it is most likely that reversal occurs by curling or nucleation followed by propagation of domain walls. The curling process is effective if the diameter D is larger than Λ but lower than the width of a Bloch wall $\Delta = (A/K)^{1/2}$, where K is the magnetic in-plane anisotropy constant. Its order of magnitude for cobalt is usually about 10^5 erg/cm³, one then obtains a value $\Delta \approx 50$ nm. Thus, this process can be involved in the magnetization reversal for the 50-nm size particles. In the case of the coarser particles, multidomains may form and the magnetization reversal may be determined by the domain-wall motion. This behavior is in agreement with the phase diagram for small magnetic spheres reported by Skomski et al. [34]. It is also noticed that for Fe nanoparticles, transition from coherent to incoherent mode reversal was observed around at $d_c = 20$ nm [35]; one consequence is then the lowering of H_c in comparison with that expected from coherent rotation model.

The low values of S , 0.055 and 0.024 for the 50 and 240-nm particles, respectively, illustrate their soft magnetic behavior. Lower saturation magnetization (55–100 emu/g) and higher coercive fields (up to 460 Oe) were reported for Co particles of sizes lying between 8 and 200 nm, synthesized by a sol-gel technique [36] while fcc Co microparticles and a mixture of fcc-hcp Co microparticles [37], exhibited similar coercive fields and squareness values to those obtained in our study. The results obtained on our 50-nm Co particles are comparable to those obtained, at low temperature (3 K), on 7-nm hcp Co nanoparticles ($M_s = 145$ emu/g and $H_c = 130$ Oe) [37]. However, a lower saturation field $H_s = 1$ kOe and a higher squareness $S = 0.45$ were reported. Indeed, the magnetic behavior depends on different parameters such as synthesis technique, temperature, particle size, and crystalline structure.

3.2.2 Consolidated samples When the magnetic field is applied normal to the sample plane (Fig. 5), the magnetization loops look like those we can expect from the usual scheme of a coherent rotation in the hard axis-geometry. The effective anisotropy field is defined as $H_{\text{eff}} = 4\pi M_{\text{eff}} = 4\pi M_s - H_{a\perp}$, where $H_{a\perp}$ is the perpendicular anisotropy field and $4\pi M_s$ is the magnetization at saturation. However, because of the grain sizes, the coherent

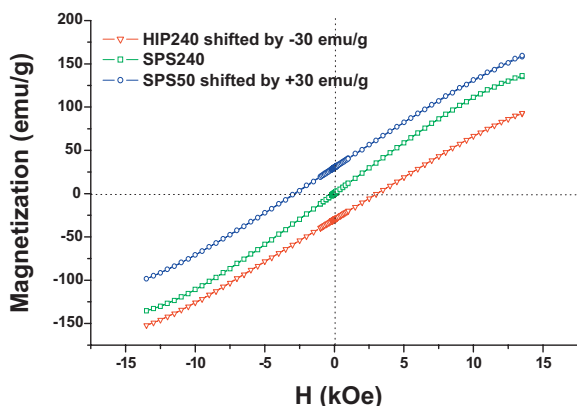


Figure 5 (online colour at: www.pss-a.com) Hysteresis loops of Co consolidated samples with the applied field H perpendicular to the sample plane obtained at room temperature ($T = 300$ K). The loops corresponding to HIP240 and SPS50 have been shifted by -30 emu/g and $+30$ emu/g, respectively.

rotation is certainly not the mechanism of magnetization reversal, but, in order to just obtain an order of magnitude of the magnetic anisotropy, one can assume a coherent reversal scheme. In this case, the slope at the origin [$M_s / (4\pi M_s - H_{a\perp})$] equal to 0.085 for HIP240, 0.089 for SPS50, and 0.093 for SPS240, leads to this information. Such a rough estimation gives the following values of $H_{a\perp}$: 1.1, 1.67, and 2.2 kOe for the HIP240, SPS50, and SPS240 samples, respectively.

These values are, as expected, weak compared to the saturation magnetization. In fact, the crystal structure is dominated by the fcc cubic phase; the contribution of the hcp phase being relatively modest, as revealed by XRD measurements. On the other hand, pole figures (not shown) revealed that the samples exhibit no marked fiber texture; those elaborated by SPS exhibiting a very small 00.2 texture. From the observed crystallographic features of the samples one then expects weak perpendicular anisotropy whose origin is probably related to magnetocrystalline and magnetoelastic contributions. It is, however, interesting to note that the samples obtained by SPS consolidation actually exhibit larger anisotropy values than the one consolidated under HIP conditions. In the first case, the nanoparticles are submitted to a uniaxial pressure that may favor anisotropy, while the effect is less marked in the second case where the pressure is isostatic.

Figure 6 displays the hysteresis curves obtained for the consolidated samples in the longitudinal configuration in an applied field up to 2.5 kOe. The insert shows the cycles for the complete field range. The coercive field H_c is found to be of same order of magnitude as for nanoparticles and to increase with the grain size, while S decreases (see Table 1). The $M-H$ loops show a linear-like decrease of the magnetization. Consequently, the values of H_c and of the squareness S are weak, characteristic of a soft magnetic behavior. For comparison, thick cobalt samples obtained by thermal deposition on silicon or glass substrate were

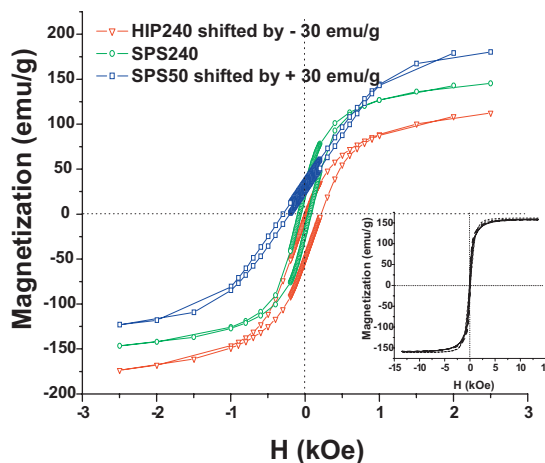


Figure 6 (online colour at: www.pss-a.com) Hysteresis loops of the consolidated samples obtained at room temperature ($T = 300$ K) with the applied field H parallel to the sample plane displayed in the $[-2.5$ kOe; $+2.5$ kOe] field range. The loops corresponding to HIP240 and SPS50 have been shifted by -30 emu/g and $+30$ emu/g, respectively. The insert shows the global hysteresis loops.

characterized by relatively large S values; the largest value, 0.754, was observed for a 195-nm thick sample [28] while a value close to 0.75 was also reported for cobalt films obtained by chemical vapor deposition [38]. Our measured values of H_c are, however, still higher than those reported for amorphous materials or for nanocrystalline materials (up to $D = 100$ nm). In the latter case, a D^6 dependence of H_c was observed [11] and successfully described within the RAM model [12]. The nanocrystalline materials fill in the gap between amorphous and conventional polycrystalline materials that exhibit large grain size, for which H_c follows a $1/D$ dependence [11]. This relation is generally ascribed to the pinning of domain walls at interfaces or grain boundaries.

The observed magnetization behavior in our samples seems to rule out pinning at the grain boundaries as the origin for the coercivity (the so-called “pinning coercivity” [39]). Moreover, small grains may favor nucleation of reverse domains. This will tend to lower the coercivity. Based on this correlation between values of coercive fields and grain size, we believe that in our case the coercivity is mainly associated with nucleation of reverse domains rather than with pinning of domain walls. Note that for bulk magnetic materials, a magnetization reversal taking place through a process of nucleation of small reversed domains (usually on inhomogeneities or defects) and a subsequent propagation of magnetic domain walls is rather reported [17]. Thus, the lamellar microstructure within grains, combined to the dipolar interactions, probably also contribute to the fast reversal mechanism observed and may induce a supplementary local anisotropy within each grain. The exact role of the observed thin microstructures needs to be clearly evidenced for further investigations.

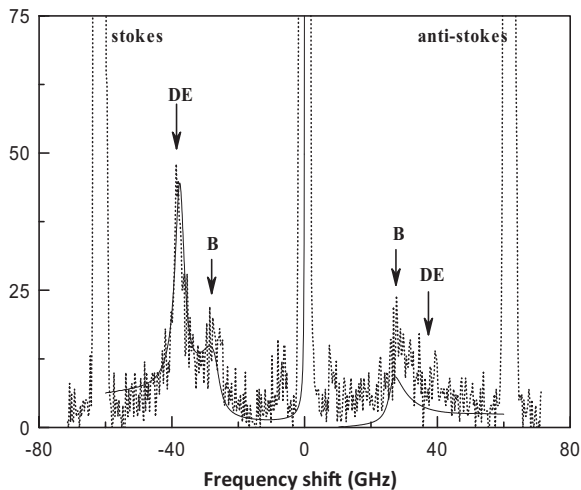


Figure 7 Typical Brillouin spectrum obtained from the sample SPS240 with an angle of incidence $q=45^\circ$ (*i.e.*, $k=1.73 \times 10^5 \text{ cm}^{-1}$) and an applied field $H=3.5 \text{ kOe}$. DE and B set for the surface-like-mode and bulk-like-mode spin waves lines, respectively. Continuous line: calculated spectrum.

3.3 Dynamic magnetic measurements Figure 7 shows a typical Brillouin spectrum obtained in the case of the SPS240 sample with an angle of incidence $\theta=45^\circ$ and an applied magnetic field $H=3.5 \text{ kOe}$. It exhibits two magnetic lines in both the Stokes (left side) and anti-Stokes (right side), namely Damon–Eshbach (DE) and B, respectively. The large Stokes/anti-Stokes intensity ratio of the DE line identifies it as a DE surface-mode-like spin wave [40]. On the other hand, the broad line B exhibits the behavior of a bulk-like-mode line, regrouping a high number of standing spin waves (SSW), which is very sensitive to the magnetic exchange within the material.

For a magnetic material of large thickness, in the dipolar approximation (absence of exchange) and neglecting anisotropy, the expression for the DE spin waves frequencies f approximates to the value [40]:

$$\frac{2\pi f}{\gamma} = (H + 2\pi M_s), \quad (1)$$

where M_s is the saturation magnetization, γ the gyromagnetic factor, and H is the applied magnetic field. In the limit of a null wave vector, the surface-wave frequency decreases and reaches the frequency of the bulk mode:

$$\frac{2\pi f}{\gamma} = \sqrt{H(H + 4\pi M_s)}. \quad (2)$$

The study of the frequency dependence of the DE and B modes on the magnetic field strength has been carried out for all the consolidated materials. Experimental and calculated curves are reported in Fig. 8 for the representative case of the SPS240 sample. The best fits of the calculated curves to the experimental points have been obtained from Eqs. (1) and (2)

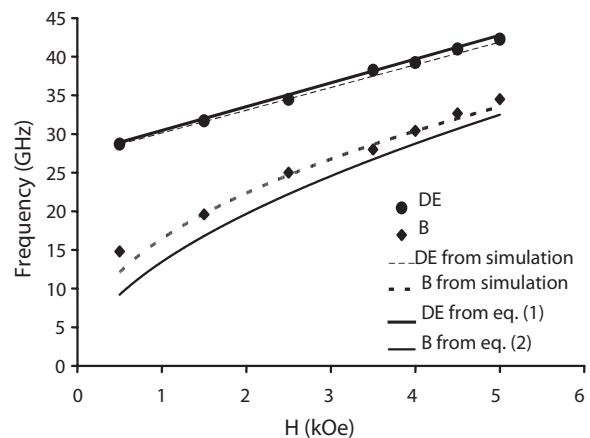


Figure 8 Variation of the DE and B modes frequency f versus the applied magnetic field H for SPS240 sample with an angle of incidence $\theta=45^\circ$ (*i.e.*, $k=1.73 \times 10^5 \text{ cm}^{-1}$). Symbols are the experimental data; the continuous lines are best fits obtained using Eq. (1) for the DE mode and (2) for the B mode with a saturation magnetization $4\pi M_s=17.6 \text{ kOe}$ and a gyromagnetic factor: $\gamma=1.9 \times 10^7 \text{ Hz/Oe}$. The dashed lines are the fits obtained from the complete simulation of the BLS spectra (see text).

for the DE and B modes, respectively, taking γ fixed at its value for bulk cobalt: $\gamma=1.95 \times 10^7 \text{ Hz/Oe}$, *i.e.*, $g=2.16$, and surprisingly by adjusting the saturation magnetization to its value for cobalt bulk material $4\pi M_s=17.6 \text{ kOe}$, indicating a vanishing magnetic anisotropy in the consolidated films. Note that the bulk B mode exhibits a less marked agreement using Eq. (2), that provides the frequency of the uniform mode. The bulk mode is sensitive to the magnetic exchange (neglected here) and then Eq. (2) represents a rough approximation of its frequency. In order to provide a better agreement between experiment and theory, a complete numerical simulation of the spectra, taking into account the magnetic exchange, has been achieved [41]. This allows the fitting of the spectra with appropriate parameters, namely, in our case, g coefficient (2.16), the magnetization at saturation $4\pi M_s$ (17.6 kOe) and the exchange stiffness constant A ($1.8 \times 10^{-6} \text{ erg/cm}$ *i.e.*, $D_{\text{ech}}=2.6 \times 10^{-9} \text{ Oe cm}^2$ with $D_{\text{ech}}=M_s A/2$ being the spin wave exchange constant), which corresponds to the values reported for polycrystalline thick cobalt films [29, 42]. For comparison, the D_{ech} value derived from our BLS measurements is 32% smaller than that obtained from a neutron-scattering study of single-crystal cobalt [43]. The polycrystalline character of our samples combined with the fact that inelastic light measurements only provide an average value for D_{ech} can explain such a discrepancy. It is indeed noteworthy that BLS measurements on single-crystalline Co films [44] have produced results closer to those obtained by the neutron-scattering study of Ref. [43]; the difference being about 13%.

Figure 8 shows the experimental frequency variations versus the applied field compared to our best fits (dashed lines), obtained using the above-determined values of the magnetic parameters.

The fitted value of the saturation magnetization confirms the assumption of a negligible magnetic anisotropy. On the other hand, it indicates that the contribution of a nonferromagnetic phase, if it exists in the grain-boundaries region, is negligible. This is also confirmed by the value of the exchange stiffness constant A that we have determined that is a strong indication that the magnetic “contact” between the particles after the consolidation process is not significantly altered, eventually, by the presence of a secondary crystalline phase (antiferromagnetic CoO phase, cobalt oxide, amorphous phase, etc.) at the grain boundaries, which could lower A . A similar feature has been recently reported on Co polycrystalline nanomaterials with an average grain size of 10 nm where no reduction in exchange stiffness has been observed despite the presence of a high volume of grain boundaries [45]. It is interesting to note that XRD measurements showed that the sample consolidated by HIP presents a more or less noticeable amount of cobalt oxide CoO (6%), whereas those consolidated by SPS are pure cobalt phases. This can be due to the difference in the elaboration protocol [21]. However, no significant variation of the fitted magnetic parameters was noticed in the case of the HIP240 sample. The CoO contribution remains negligible. As pointed out in the introduction, indeed the exchange coupling between the grains depends on the magnetic nature of the intergranular region, as observed in multiphase systems [11]. Studies of collective spin waves in $\text{Co}_{100-x}\text{Cr}_x$ alloy films by means of BLS at room temperature [46, 47] reported a strong reduction of the magnetic exchange constant when the Cr content increases, a value of $D_{\text{ech}} = 0.75 \times 10^{-9} \text{ erg cm}^2$ has been obtained for example for $x = 15.7 \text{ at\%}$, almost four times lower than the bulk value [46] while a reduction by an order of magnitude was found for Cr content reaching 50 at% [47]. The segregation of nonmagnetic Cr along grain boundaries was discussed as the possible origin of this drastic reduction. Thus, we can infer that the consolidation routes used in this work insure a good magnetic interfacial contact between the particles.

4 Conclusions The static and dynamic properties of Co nanoparticles and subsequently consolidated samples were studied. The static magnetization behavior is found to be characteristic of a soft magnetic material showing weak values of the squareness and of the coercive field. The magnetization behavior seems to obey a nucleation/propagation scheme. A curling process can, however, be involved in the magnetization reversal for the smaller (50-nm size) particles. In fact, based on the correlation between values of coercive fields and grain size, we believe that the coercivity is mainly associated with nucleation of reverse domains rather than with pinning of domain walls. The lamellar microstructure could also influence the grain-size dependence of coercivity. The structural and dynamic properties, confirm that the samples exhibit a vanishing magnetic anisotropy. The intergranular region seems to not alter the magnetic exchange between the grains, as is deduced from

the obtained values of the magnetization at saturation and of the exchange stiffness constant.

Acknowledgements This work was conducted in the framework of an interdisciplinary research program at LPMTM. K. B. is very grateful to the University of Paris 13 for the stay as a visiting Professor.

References

- [1] J. L. Dormann and D. Fiorani, *Magnetic Properties of Fine Particles* (North-Holland, New York, 1992).
- [2] H. Gleiter, *Nanostruct. Mater.* **6**, 3 (1995).
- [3] T. G. Langdon, *Mater. Sci. Eng. A* **462**, 3 (2007).
- [4] F. Wetscher, A. Vorhauer, and R. Pippan, *Mater. Sci. Eng. A* **410/411**, 213 (2005).
- [5] U. Erb, *Nanostruct. Mater.* **6**, 533 (1995).
- [6] R. Hasegawa, *J. Non-Cryst. Solids* **329**, 1 (2003).
- [7] C. Rizkallah, J. P. Fondère, H. F. Raynaud, and A. Vignes, *Cahier d'Informations Techniques/Sciences et Génie des Matériaux* (Edition Diffusion Presse (EDP) Sciences, France, 2001), p. 1109.
- [8] B.-N. Kim, K. Hiraga, K. Morita, and H. Yoshida, *Scr. Mater.* **57**, 607 (2007).
- [9] J. A. Bas, J. A. Calero, and M. J. Dougan, *J. Magn. Magn. Mater.* **254/255**, 391 (2003).
- [10] J. Füzér, J. Bednárčík, P. Kollár, and S. Roth, *J. Magn. Magn. Mater.* **316**, e834 (2007).
- [11] G. Herzer, *Scr. Metall. Mater.* **33**, 1741 (1995).
- [12] G. Herzer, *IEEE Trans. Magn.* **26**, 1397 (1990).
- [13] R. Alben, J. J. Becker, and M. C. Chi, *J. Appl. Phys.* **49**, 1653 (1978).
- [14] J. P. Perez, V. Dupuis, J. Tuaille, A. Perez, V. Paillard, P. Melinon, M. Treilleux, L. Thomas, B. Barbara, and B. Bouchet Fabre, *J. Magn. Magn. Mater.* **145**, 74 (1995).
- [15] J. F. Löffler, J. P. Meier, B. Doudin, J.-P. Ansermet, and W. Wagner, *Phys. Rev. B* **57**, 2915 (1998).
- [16] F. Pfeifer and C. Radloff, *J. Magn. Magn. Mater.* **19**, 190 (1980).
- [17] J. Vogel, J. Moritz, and O. Fruchart, *C. R. Phys.* **7**, 977 (2006).
- [18] H. E. Schäfer, H. Kisker, H. Kronmüller, and R. Würsum, *Nanostruct. Mater.* **1**, 523 (1992).
- [19] H. Kisker, T. Gessmann, R. Würsum, H. Kronmüller, and H. E. Schäfer, *Nanostruct. Mater.* **6**, 925 (1995).
- [20] F. Fellah, G. Dirras, J. Gubicza, F. Schoenstein, N. Jouini, S. M. Chérif, C. Gatel, and J. Douin, *J. Alloys Compd.* **489**, 424 (2010).
- [21] F. Fellah, F. Schoenstein, A. Dakhlaoui-Omrani, S. M. Cherif, G. Dirras, and N. Jouini, *J. Alloys Compd.* (to be published).
- [22] L. Poul, S. Ammar, N. Jouini, F. Fievet, and F. Villain, *J. Sol-Gel Sci. Technol.* **26**, 261 (2003).
- [23] S. O. Demokritov and E. Tsymbal, *J. Phys. C* **6**, 7145 (1994).
- [24] N. A. Sergeeva, S. M. Chérif, A. A. Stashkevich, M. P. Kostylev, and J. Ben Youssef, *J. Magn. Magn. Mater.* **288**, 250 (2005).
- [25] M. J. N. V. Prasad, S. Suwas, and A. H. Chokshi, *Mater. Sci. Eng. A* **503**, 86 (2009).
- [26] Z. Zhang, X. Chen, X. Zhang, and C. Shi, *Solid State Commun.* **139**, 403 (2006).
- [27] X. M. Liu and Y. C. Zhou, *J. Cryst. Growth* **270**, 527 (2004).

- [28] A. Dakhlaoui, M. Jendoubi, L. S. Smiri, A. Kanaev, and N. Jouini, *J. Cryst. Growth* **311**, 3989 (2009).
- [29] A. Kharmouche, S. M. Chérif, A. Bourzami, A. Layadi, and G. Schmerber, *J. Phys. D: Appl. Phys.* **37**, 2583 (2004).
- [30] A. Dakhlaoui Omrani, M. A. Bousnina, L. S. Smiri, M. Taibi, P. Leone, F. Schoenstein, and N. Jouini, *Mater. Chem. Phys.* **123**, 821 (2010).
- [31] D. L. Leslie-Peleckly and R. D. Rieke, *Chem. Mater.* **8**, 1770 (1996).
- [32] A. Aharoni, *Introduction to the Theory of Ferromagnetism* (Oxford University Press, Oxford Science Publications, UK 1996).
- [33] E. Koerster and T. C. Arnoldussen, *Magnetic Recording*, Vol. 1, edited by C. D. Mee and E. D. Daniel (McGraw-Hill, New York, USA, 1987).
- [34] R. Skomski, A. Kashyap, K. D. Sorge, and D. J. Sellmyer, *J. Appl. Phys.* **95**, 7022 (2004).
- [35] T. Ibusuki, S. Kojima, O. Kitakami, and Y. Shimada, *IEEE Trans. Magn.* **37**, 2223–2225 (2001).
- [36] H. Shao, Y. Huang, H. S. Lee, Y. J. Suh, and C. O. Kim, *J. Magn. Magn. Mater.* **304**, e28 (2006).
- [37] Q. Yuanchun, Z. Yanbao, and W. Zhishen, *Mater. Chem. Phys.* **110**, 457 (2008).
- [38] N. Deo, M. F. Bain, J. H. Montgomery, and H. S. Gamble, *J. Mater. Sci.: Mater. Electron.* **16**, 387 (2005).
- [39] M. Rossignol, *Magnétisme, I. Fondements*, under the direction of Etienne du Trémolet de Lacheisserie (Presses Universitaires de Grenoble, France, 1999).
- [40] R. W. Damon and J. R. Eshbach, *J. Phys. Chem. Solids* **19**, 308 (1961).
- [41] Y. Roussigné, F. Ganot, C. Dugautier, P. Moch, and D. Renard, *Phys. Rev. B* **52**, 350 (1995).
- [42] S. P. Vernon, S. M. Lindsay, and M. B. Stearns, *Phys. Rev. B* **29**, 4439 (1984).
- [43] G. Shirane, V. J. Minkiewicz, and R. Nathan, *J. Appl. Phys.* **39**, 383 (1968).
- [44] X. Liu, M. M. Steiner, R. Sooryakumar, G. A. Prinz, R. F. C. Farrow, and G. Harp, *Phys. Rev. B* **53**, 12166 (1996).
- [45] D. Honecker, F. Döbrich, C. D. Dewhurst, A. Wiedenmann, and A. Michels, *J. Phys.: Condens. Matter* **23**, 016003 (2011).
- [46] A. Yoshihara, H. Sato, J.-I. Chi Mawatari, K. Yoshida, O. Kitakami, and Y. Shimada, *J. Magn. Magn. Mater.* **221**, 261 (2000).
- [47] A. Kharmouche, S. M. Chérif, G. Schmerber, and A. Bourzami, *J. Magn. Magn. Mater.* **310**, 152 (2007).